# Electron *g*-factor engineering for nonreciprocal spin photonics

Parijat Sengupta,[1] Chinmay Khandekar,[1] Todd Van Mechelen,[1] Rajib Rahman [2] and Zubin Jacob[1,*]

[1]*Department of Electrical and Computer Engineering and Birck Nanotechnology Center, Purdue University, West Lafayette, Indiana 47907, USA*

[2]*School of Physics, University of New South Wales, Sydney, New South Wales 2052, Australia*

We study the interplay of electron and photon spin in nonreciprocal materials. Traditionally, the primary mechanism to design nonreciprocal photonic devices has been magnetic fields in conjunction with magnetic oxides, such as iron garnets. In this work, we present an alternative paradigm that allows tunability and reconfigurability of the nonreciprocity through spintronic approaches. The proposed design uses the high spin-orbit coupling (SOC) of a narrow-band-gap semiconductor (InSb) with ferromagnetic dopants. A combination of the intrinsic SOC and a gate-applied electric field gives rise to a strong external Rashba spin-orbit coupling (RSOC) in a magnetically doped InSb film. The RSOC which is gate alterable is shown to adjust the magnetic permeability tensor via the electron *g* factor of the medium. We use electronic band structure calculations (k · p theory) to show that the gate-adjustable RSOC manifest itself in the nonreciprocal coefficient of photon fields via shifts in the Kerr and Faraday rotations. In addition, we show that photon spin properties of dipolar emitters placed in the vicinity of a nonreciprocal electromagnetic environment are distinct from reciprocal counterparts. The Purcell factor ($F_p$) of a spin-polarized emitter (right-handed circular dipole) is significantly enhanced due to a larger *g* factor while a left-handed dipole remains essentially unaffected. Our search for novel nonreciprocal material platforms can lead to electron-spin-controlled reconfigurable photonic devices.

## I. INTRODUCTION

Nonreciprocal photonic materials such as ferrites and magnetized plasmas are central to the design of optical isolators and circulators [1]. While technology exists in the microwave regime, there is a major impetus driving on-chip miniaturization of nonreciprocal devices for quantum [2] as well as classical [3] applications. A particular frontier in this regard is time modulation to achieve nonreciprocity as an alternative to using magnetic materials. However, significant challenges remain—primarily, insertion loss and the high-speed modulation of such effects—which makes it an area of active interest in which to carry out a search for new materials exhibiting nonreciprocity.

There is an intimate connection between photon spin and nonreciprocal materials exhibiting gyrotropy. A classical analysis [4] of gyrotropic media [5] reveals that the eigenstates of such a medium are circularly polarized with differing phase velocities. However, the role of spin in the near field of gyrotropic media has not been fully analyzed. In this work, we put forth approaches to probe the near-field spin properties of nonreciprocal media. We note here that the special case of moving media which displays magnetoelectric nonreciprocity has spin-split mode dispersion [6].

Recently, gyrotropy was demonstrated to be equivalent to effective photon mass through a direct comparison with an optical analog of the Dirac equation [7–9]. Gyrotropy inside matter has properties similar to Dirac mass and is accompanied by a low-energy (frequency) band gap for propagating electromagnetic waves. Within this electromagnetic band gap, Maxwellian spin waves can exist with unidirectional propagation and are closely related to Jackiw-Rebbi waves that occur at the interface of positive and negative mass media. In addition, there can exist a topological electromagnetic phase of atomic matter [10,11] that arises from nonlocal gyrotropy which is a spatiotemporally dispersive Hall conductivity. This gyroelectric phase of atomic matter [10,11] achieves skyrmionic texture of photonic spins in momentum space [9]. The nonlocal topological electromagnetic phase can host helicity-quantized unidirectional [12] edge waves fundamentally different from classical magneto-plasmons. This advancement illustrates how hitherto unexplored forms of gyrotropy can lead to creation of intriguing Maxwellian spin waves as well as spin-1 photonic skyrmionic textures.

An equally fundamental application of nonreciprocal materials lies in controlling radiative heat transport [13,14]. Thermal photonic energy density in the near field of a planar slab of gyrotropic media has been predicted to show unidirectional transport behavior even under equilibrium conditions [14]. This effect arises from universal spin-momentum locking of evanescent waves [15] in the near field of a nonreciprocal slab. Topological electronic materials that exhibit nonreciprocity such as Weyl semimetals and axion insulators are ideal for verifying concepts of thermal spin photonics [14].

The focus of this paper is electron-spin control of gyrotropy which utilize spintronic devices for applications requiring photonic nonreciprocity. Typically, conventional gyroelectric media rely on cyclotron orbits and orbital angular

momentum of electrons interacting with a fixed magnetic field; gyromagnetic media, on the other hand, obtain their nonreciprocal behavior from electron-spin angular momentum interaction with the static magnetic bias. These materials are also widely known as magneto-optic media. Here, we couple band structure calculations—performed using an eight-band k · p Hamiltonian adapted [16] to quantum wells—to the theory of magnetic permeability tensors. This approach leads to a computation of the nonreciprocity coefficient inside matter for photon fields.

We propose nanoscale thick InSb quantum well structures [17] exhibiting optical nonreciprocity. Our structures are more amenable to use in small-sized integrated systems and unlike YIG, the growth of quantum well devices is established easily through molecular beam epitaxy. We emphasize that leveraging the spin of the electron with a gate field for nonreciprocal photonics remains unexplored heretofore. InSb has been previously explored [18] for its nonreciprocity with emphasis on its gyroelectric behavior; the present work shows that it is possible to design "multigyroic" materials which have nonreciprocity in both the electric and magnetic off-diagonal permeability and susceptibility tensor components. We further note that while similar analyses with gyroelectric media exist in the literature [1,19] wherein nonreciprocity has been demonstrated [20], such realizations are generally incumbent solely upon the external magnetic field and offer no recourse to further modulations via microscopic device rearrangements. For clarity, throughout the paper, we do not invoke the terminology of chirality [21]. Chirality (i.e., traditional optical activity) is a reciprocal phenomenon, and the fields of metamaterials, plasmonics, and chemistry define it as a coupling coefficient of electric and magnetic fields. Gyrotropic nonreciprocity, in contrast, associated with photon spin inside matter, couples the orthogonal components of the electric (or magnetic) fields.

The present work, as mentioned above, combines a large spin-orbit coupling, narrow band gap, and crystalline asymmetry of the target nanostructure, materializing in a significant external Rashba spin-orbit field [22,23]. This effectively changes the material response to an impinging light beam in the presence of an external magnetic field which is discernible from appropriate magneto-optical data. We now give a succinct description of the arrangement on which the theoretical and computational analysis of the latter sections is centered. The model structure is a magnetically doped InSb [Fig. 1(a)] slab with a permanent axis of magnetization (**M**) normal (aligned to the z axis) to the x-y plane and forms the optically active component. The slab [Fig. 1(a)] is also placed under an external magnetic field parallel to **M** while a gate electrode is affixed to the top. The nonreciprocity of the magnetized InSb slab is captured by the nonzero off-diagonal elements in the permeability ($\mu$) tensor matrix. However, beyond the influence of the magnetic fields, the extent to which such nonreciprocity manifests is also functionally dependent on the gyromagnetic ratio [$\gamma = g(e/2m_e^*)$]. Here, $e$ stands for the electronic charge and $m_e^*$ is the effective electron mass. The g factor, therefore, evidently via $\gamma$ determines the solutions to Maxwell's equations that govern the light-matter interaction in this setup. The middle panel [Fig. 1(b)] denotes this process wherein a tailorable g factor arises as the
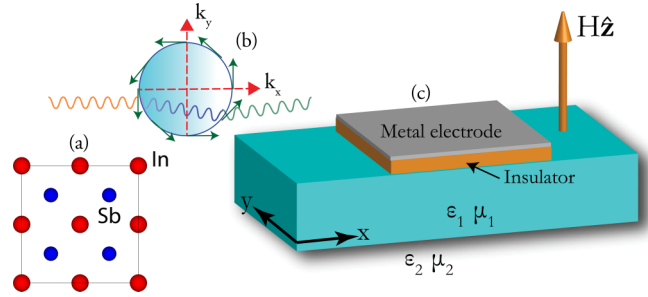


FIG. 1. The schematic represents the arrangement considered in this work. The left panel (a) shows a unit cell of ferromagnetically doped InSb (red atom denotes In while blue stands for Sb) irradiated with a beam of light (wavy line) that traverses its body and emerges on the opposite side. The passage of the light beam is governed by the constitutive parameters, $\epsilon_1$ and $\mu_1$, of InSb, which is gyrotropic with an inherent magnetization. Note that for gyrotropy to be observed, an out-of-plane magnetic field (Hz) is applied to the device. The permeability tensor in this case is significantly modified by the external Rashba spin-orbit coupling (RSOC) that exists on the InSb slab. The amplitude of transmission of an incident beam through the slab, marked as an angled wavy blue line in the middle panel (b), is therefore linked to the strength of the RSOC. The RSOC in (b) is identified by its characteristic spin-momentum locking, where the tangential green lines indicate the spin-polarization vectors. The right panel (c) is a possible realization of a gyrotropic and nonreciprocal optical device. It is fitted with a metal gate that allows a dynamic tuning of RSOC, leading to the necessary modulation of the light beam. We elucidate here, via demonstration of such optical control, an indirect but robust connection between the electron spin and diverse photonic applications.

light beam propagates through a medium with significant external Rashba field identified through the spin-momentum locked states on an equienergy circular contour. As tangible illustrations of such synergy—albeit indirect—between a photon beam and the Rashba spin-orbit coupling (RSOC), we show (1) variations in the characteristic magneto-optical measurements, in particular, the Kerr and Faraday rotation with a varying electric field, and (2) the Purcell factor of nonreciprocal photon spin-polarized dipole emission.

Briefly, we note that changes to the Rashba coupling parameter ($\lambda_R$) through a gate electric field and the dispersion relation (through additional confinement and strain, etc.) revise the g-factor profile—a higher $\lambda_R$ leading to an enhanced value, and revealed as greater Kerr and Faraday rotations [24]. We also show electron-spin control of the photon-spin-dependent Purcell factor [25,26]. Before we proceed to a complete analysis of the g-factor engineered nonreciprocal phenomena, a note about the organization of the paper is in order: In Sec. II steps are outlined for the g-factor calculation beginning with the model Hamiltonian for the InSb slab; this is followed by a quantitative discussion on electron spin-orbit coupling governed Kerr and Faraday rotations that characterize the viability of nonreciprocity-driven magneto-optical devices (Sec. III). The Purcell factor and its numerical determination are taken up next in Sec. IV, and we close by summarizing the key findings in Sec. V, which also touches on the possibilities of extending the current work to include aspects of material and structural optimization.

## II. THEORY

The basis of all calculations presented in this paper begins with two essential steps: (1) constructing the permeability ($\mu$) tensor matrix that ties its behavior to the extrinsic Rashba spin-orbit coupling, and (2) band dispersion of the two-dimensional (2D) ferromagnet. In this section, their analytic expressions are presented in the same order below. Note that at this stage the steps are generalized and no target material is specified; however, we will allude to possibilities during a numerical evaluation of the $\mu$ matrix and the overall band dispersion later in the paper.

We begin by writing the Landau-Lifshitz equation that governs all magnetization (**M**) behavior in a magnet. In the presence of Gilbert damping, and in an external magnetic field (**H**), it takes the form [27,28]

$$\frac{\partial M}{\partial t} = \gamma \mu_0 (M \times H) + \frac{\alpha \gamma}{M}[M \times (M \times H)], \qquad (1)$$

where

$$\gamma = \frac{ge}{2m_e^*}. \qquad (2)$$

In Eq. (1), $g$ is the Landé factor, $m_e^*$ is the electron's effective mass, and $\alpha$ is the Gilbert damping. The magnetic permeability in vacuum is $\mu_0$. Without loss of generality, we let the magnetic field vector point along the $z$ axis and superimpose a small and identically directed ac field, $H' \exp(i\omega t)$. The ac field imparts a frequency dependence to the structure of the $\mu$ tensor matrix. Analogously, the **M** vector is also assumed to point along the $z$ axis in addition to an induced ac component, $M' \exp(i\omega t)$. Inserting the complete expressions for the magnetization and magnetic field in Eq. (1), the tensor components assume the form [29]

$$\overline{\overline{\mu}} = \begin{pmatrix} \mu_{xx} & -i\kappa_{xy} & 0 \\ i\kappa_{xy} & \mu_{xx} & 0 \\ 0 & 0 & \mu_{zz} \end{pmatrix}, \qquad (3)$$

where the individual entries are defined as

$$\mu_{xx} = 1 + \frac{(\omega_0 + i\alpha\omega)\omega_m}{(\omega_0 + i\alpha\omega)^2 - \omega^2},$$

$$\kappa_{xy} = -\frac{\omega\omega_m}{(\omega_0 + i\alpha\omega)^2 - \omega^2}. \qquad (4)$$

Finally, $\mu_{zz} = 1 + M/H$, $\omega_m = \gamma\mu_0 M$, and $\omega_0 = \gamma\mu_0 H$. This completes the form of the tensor matrix for a gyromagnetic material. A set of remarks is in order here: First, we note the structure of the $\mu$ matrix in Eq. (4), whose off-diagonal elements vanish (the medium therefore turns isotropic, assuming no gyroelectricity is present) in absence of **M**, the intrinsic magnetization vector. Additionally, it is a Hermitian tensor, since $\mu_{ik} = \mu_{ki}^*$. The next comment pertains to the matrix dependence on the electron $g$ factor via the gyromagnetic ratio ($\gamma$), a number that is manifestly material driven; as a case in point, it is determined to be $-0.44$ for GaAs [30] conduction electrons while reaching $\approx 50$ in 2D InSb [31]. Notice that the free-electron value of $g = 2.0023$ does not apply for a crystal. The $g$ factor of an electron bound to a lattice, *inter alia*, is primarily governed by the intrinsic spin-orbit coupling (SOC) and therefore must be computed for each nanosystem including the appropriate quantization

effects, which are reflected via the dispersion (electronic) relations through altered (from bulk values) band gaps and effective masses. We will expound on this point in greater detail in the following subsection and present a path that ties SOC effects and their influence on the overall nonreciprocal behavior.

### Determination of the *g* factor

We remarked above on the functional relationship between the structure of the $\mu$ tensor and crystal SOC. In what follows, we make explicit use of band dispersion to formalize this connection. We consider an InSb slab which crystallizes under zinc-blende symmetry and displays a substantial RSOC. A minimal Hamiltonian representing the $\Gamma_6$ conduction bands under RSOC is expressed as

$$H_0 = \frac{p^2}{2m^*} + \lambda_R(\sigma_x k_y - \sigma_y k_x), \qquad (5)$$

where $\lambda_R > 0$ is the Rashba coupling parameter. The effective mass in Eq. (5) is $m^*$. In the presence of a $z$-directed magnetic field, carrying out the usual Peierl's transformation, the momentum terms are rewritten as $\hbar k \to \hbar k - e\mathbf{A}(t)$, where **A** is expressed by a Landau gauge of the form $(0, B_z x, 0)$. The momentum terms in Eq. (5), following this change, can be expressed via creation ($a^\dagger$) and annihilation ($a$) operators, $k_+ = k_x + ik_y = \sqrt{2}/l_B a^\dagger$ and $k_- = k_x - ik_y = \sqrt{2}/l_B a$, while $k^2$ is now $0.5(k_+k_- + k_-k_+) = \frac{2}{l_B^2}(a^\dagger a + \frac{1}{2})$. Here, $l_B = \sqrt{\hbar/eB_z}$, the magnetic length.

It is now straightforward to diagonalize the Hamiltonian to obtain the eigenstate for the $n$th quantum level; it is simply

$$\mathcal{E}_n = \frac{\hbar eB}{m^*}n \pm \sqrt{\left(\Delta - \frac{\hbar eB}{2m^*}\right)^2 + \frac{2ne\lambda_R^2 B}{\hbar}}. \qquad (6)$$

The term $\Delta = \frac{1}{2}g_0\mu_B B$ accounts for the Zeeman splitting of spin states in a $z$-axis pointed magnetic field. Note that we set $g_0 = 2.0$ and $\mu_B$ is the standard Bohr magneton. The upper (lower) sign is for the spin-up (spin-down) electron. The effective $g$ factor that an electron experiences can then be approximated as

$$g_{\text{eff}} = \frac{\mathcal{E}_1 - \mathcal{E}_{-1}}{2\mu_B B}. \qquad (7)$$

Notice that we limit our analysis to the $n = 1$ Landau level for the computation of the effective $g$ factor. In Fig. 2, the Landau levels (up to $n = 8$) are shown; in addition, the difference in energies between the spin-up and spin-down states for the $n = 1$ level is marked on the plot—the precise quantity desired in Eq. (7) to ascertain the $g$ factor.

As a way of elucidation, an additional comment must be included here: The $g$ factor, evidently a function of the Rashba parameter, influences the $\mu$ tensor [Eq. (4)] and the concomitant magnetic-anisotropy-linked optical phenomena. In particular, supplementary degrees of freedom in optical manipulation can manifest through alterations made to the strength of the Rashba coupling coefficient, which is $\lambda_R = \lambda_0 \langle E(z) \rangle$. Here, $\langle E(z) \rangle$ serves as the average electric field.
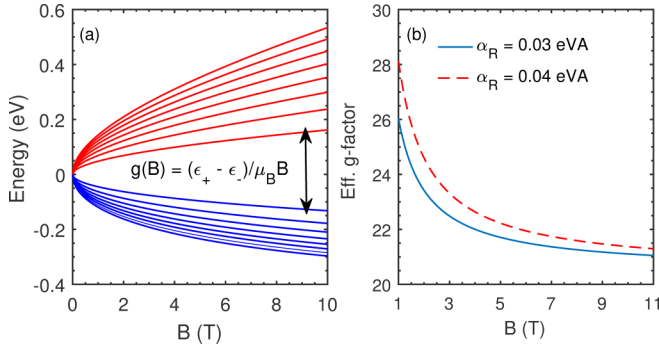
FIG. 2. The Landau dispersion for the conduction electrons of a 15.0 nm InSb slab for several values of an external $z$-axis directed magnetic field is shown here. The left panel (a) was prepared by diagonalizing the Hamiltonian; the desired InSb band parameters such as the effective mass and the fundamental band gap were obtained from an $8 \times 8$ $k \cdot p$ Hamiltonian adapted for slablike structures. A note about the band structure calculations and their numerical implementation can be found in the Appendix and Ref. [16]. The upper (lower) set of curves in red (blue) denotes the dispersion of the spin-up (spin-down) conduction electrons. The right panel (b) is the effective $g$ factors of the conduction electrons computed directly from the Landau dispersion curves. They are shown for two values of the Rashba parameter, a dynamically tunable quantity, an attribute which we harness to describe the coupling between electron spin and optical nonreciprocity in this paper.

The material-dependent $\lambda_0$ is given as [32]

$$\lambda_0 = \frac{\hbar^2}{2m^*} \frac{\Delta_{so}}{E_g} \frac{2E_g + \Delta_{so}}{(E_g + \Delta_{so})(3E_g + 2\Delta_{so})}. \qquad (8)$$

In Eq. (8), the fundamental band gap is $E_g$ and $\Delta_{so}$ denotes the intrinsic spin-orbit coupling. It is therefore easy to see how a tuning of the essential dispersion parameters—principally, the band gap and electron effective mass—can adjust $\lambda_R$ and thereby the electric and magnetic response of the system. Elucidating further, the electromagnetic response forms the solution to Maxwell's equations that are reliant on the electric permittivity and magnetic permeability of the medium, of which the latter in our case can be transformed via the RSOC-assisted $g$ factor. The set of plots [Fig. 2(b)] reinforces this reasoning. Before we proceed to discuss magneto-optical setups harnessing the embedded utility of the $g$ factor, an explanatory set of statements must be added to dispel any ambiguity: The $g$ factor is typically a tensor quantity and direction dependent; however, for the case shown here, we assumed the electrons are located at the base of the conduction band, which is spherically symmetric ($\Gamma_6$), allowing a single number to fully represent this inherent tensor quantity. For methods that carry greater rigor and include contributions from higher-energy bands, see for example, Refs. [33,34], a more accurate modeling of the $g$ factor is possible. The Appendix contains a brief note on this point. Lastly, observe that Landau levels derived from a pure parabolic model ($\lambda_R = 0$) ensure that the $g$ factor is independent of the magnetic field; the dependence here otherwise (Fig. 2) is simply an outcome of including a linear Rashba spin-orbit Hamiltonian.
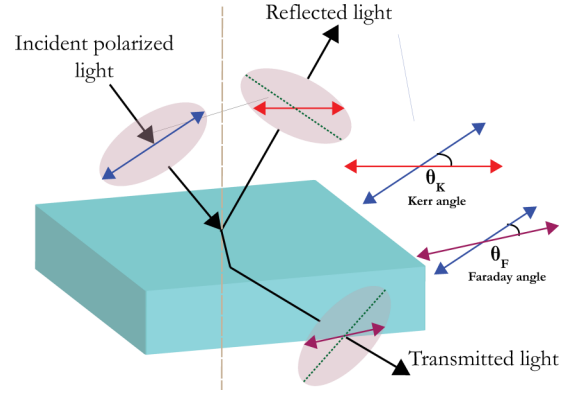


FIG. 3. The twin optical phenomena of Kerr and Faraday rotation is shown here. The solid lines contained within the ellipses represent the polarization axes which suffer rotation (drawn separately with respective angles marked as $\theta_K$ and $\theta_F$) as an incident light beam on the InSb slab is partly reflected and transmitted. Note that this configuration describes the polar magneto-optical Kerr effect (PMOKE) where the magnetization (**M**) is oriented normal to the plane.

## III. MAGNETO-OPTICAL PHENOMENA

A wide variety of functionalities can be accomplished through the inclusion of nonreciprocal photonic devices; however, as we pointed in the opening paragraphs, geometric considerations hinder integration into silicon photonic systems necessitating the need for planar and dimensionally shrunken devices. While magnetic oxide films have been put forward as suitable material systems in this regard, here we seek to explore a class of strongly spin-orbit coupled and narrow-band-gap zinc-blende materials with embedded magnetic impurities (cf. Fig. 1). The usefulness of a magneto-optical material is typically gauged by a figure of merit ($\xi$) defined as [35] Faraday degree of rotation per dB absorption; more concisely, $\xi = \theta_F/\zeta$, where $\theta_F$ is the Faraday rotation and $\zeta$ gives the absorption coefficient (per unit length) of the material. It may therefore appear prudent to measure $\theta_F$ and the related Kerr rotation ($\theta_K$) in the InSb-based setup taken up in this work. The Kerr and Faraday rotation are sketched in Fig. 3. A numerical calculation of $\theta_F$ and $\theta_K$ can be carried out by examining the Fresnel coefficients. In matrix form, for Kerr rotation, we have [36]

$$\begin{pmatrix} E_r^p \\ E_r^s \end{pmatrix} = \begin{pmatrix} r_{pp} & r_{ps} \\ r_{sp} & r_{ss} \end{pmatrix} \begin{pmatrix} E_i^p \\ E_i^s \end{pmatrix}. \qquad (9)$$

Here, $r_{ss}$, $r_{sp}$, $r_{ps}$, and $r_{pp}$ are the Fresnel coefficients and the superscript $s$ ($p$) stands for $s$ ($p$)–polarized incident ($i$) and reflected ($r$) electric field. A similar equation can be written connecting the incident and transmitted components of the electric field by introducing another set of Fresnel coefficients, which are $t_{ss}$, $t_{sp}$, $t_{ps}$, $t_{pp}$. Note that in this nomenclature, the off-diagonal coefficients ($r_{sp}$, $r_{ps}$, $t_{sp}$, $t_{ps}$) point to the intermixing of the $s$ and $p$ components. We can numerically ascertain the reflection and transmission behavior for a completely generalized case of a planar stratified and bi-anisotropic media

that follows the constitutive relations [37]

$$\mathbf{D} = \overline{\overline{\varepsilon}} \varepsilon_0 \mathbf{E} + \overline{\overline{\xi}} \frac{1}{c} \mathbf{H},$$

$$\mathbf{B} = \overline{\overline{\zeta}} \frac{1}{c} \mathbf{E} + \overline{\overline{\mu}} \mu_0 \mathbf{H}. \tag{10}$$

For our case, we set the magneto-electric coupling tensors, $\overline{\overline{\xi}}$ and $\overline{\overline{\zeta}}$, to zero while $\overline{\overline{\varepsilon}}$ and $\overline{\overline{\mu}}$ are the dimensionless permittivity and permeability tensors. The permeability tensor has nonzero off-diagonal components. The incident, reflected, and transmitted fields are then obtained by matching tangential components at the interface, which here straddles the vacuum and the InSb slab. The electric fields must therefore be computed, which we do by first writing the complete wave vector [$\mathbf{k} = (\mathbf{k}_\parallel, \pm k_z)$] expression for the reflected and incident plane waves consisting of their respective conserved parallel ($\mathbf{k}_\parallel$) and perpendicular ($\pm k_z$) components. The "+" and "−" signs indicate waves propagating away and toward the interface, respectively.

A simple application of Maxwell's equations gives the dispersion relation $k_\parallel^2 + k_z^2 = k_0^2 = (\omega/c)^2$, where $k_\parallel = |\mathbf{k}_\parallel|$ is real while $k_z$ can assume both real ($k_\parallel < k_0$) and complex ($k_\parallel > k_0$) values. Note that $\mathbf{k}_\parallel = (k_\parallel \cos\phi, k_\parallel \sin\phi)$, where $\phi$ is the angle subtended by $\mathbf{k}_\parallel$ with the $x$ axis. With this notation in mind, we substitute the ansatz $[\mathbf{E}, \sqrt{\frac{\mu_0}{\varepsilon_0}} \mathbf{H}]^T e^{i(\mathbf{k}_\parallel \cdot \mathbf{R} + k_z z - i\omega t)}$ in Maxwell's equations [Eq. (10)] to construct the following dimensionless dispersion relation inside the material:

$$\det(M + M_k) = 0, \quad \text{for } M = \begin{bmatrix} \overline{\overline{\varepsilon}} & \overline{\overline{\zeta}} \\ \overline{\overline{\xi}} & \overline{\overline{\mu}} \end{bmatrix}. \tag{11}$$

The matrix, $M_k$, is defined by the auxiliary relation

$$M_k = \begin{bmatrix} 0 & \overline{\overline{\mathbf{k}}}/k_0 \\ -\overline{\overline{\mathbf{k}}}/k_0 & 0 \end{bmatrix},$$

$$\overline{\overline{\mathbf{k}}} = \begin{bmatrix} 0 & -k_z & k_\parallel \sin\phi \\ k_z & 0 & -k_\parallel \cos\phi \\ -k_\parallel \sin\phi & k_\parallel \cos\phi & 0 \end{bmatrix}. \tag{12}$$

The $6 \times 6$ material tensor $M$ expresses the constitutive relations and $M_k$ encapsulates the result of the curl operator on the plane waves. For a completely generalized anisotropic system, we obtain $k_z$ numerically by setting $\det[M + M_k(k_z)] = 0$ for a given $(k_\parallel, \phi)$. The fields inside the material are linear combinations of these eigenstates described by polarization vectors $\hat{\mathbf{e}}_{j\pm}$ for $j = \{s, p\}$ given as

$$\hat{\mathbf{e}}_{s\pm} = \begin{bmatrix} \sin\phi \\ -\cos\phi \\ 0 \end{bmatrix}, \quad \hat{\mathbf{e}}_{p\pm} = \frac{-1}{k_0} \begin{bmatrix} \pm k_z \cos\phi \\ \pm k_z \sin\phi \\ -k_\parallel \end{bmatrix}. \tag{13}$$

The upper (lower) sign is for a wave propagating along the $+\hat{\mathbf{e}}_z$ ($-\hat{\mathbf{e}}_z$) direction. It is now a straightforward task to calculate the Faraday and Kerr rotation by simply noting the appropriate ratios of the Fresnel coefficients. For Faraday (F) and Kerr (K) rotation, we have [38]

$$\Theta_F = \theta_F + i\eta_F = \frac{t_{ps}}{t_{ss}}, \quad \Theta_K = \theta_K + i\eta_K = \frac{r_{ps}}{r_{ss}}, \tag{14}$$
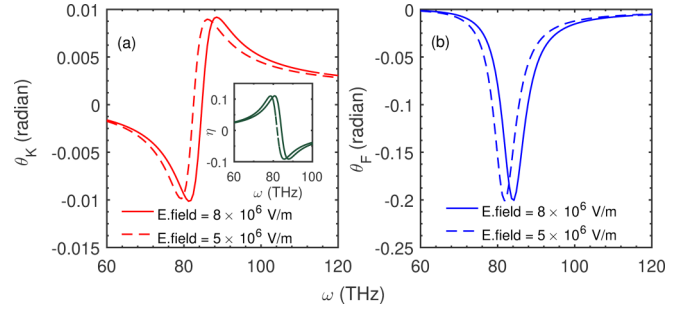


FIG. 4. We numerically calculate the Kerr (a) and Faraday (b) rotation which arises from reflected and transmitted rays for two gate fields and several incoming frequencies. The incident light is assumed to make an angle of $\pi/4$ with the normal to the plane of incidence. A higher electric field (which augments the $g$ factor) widens the Kerr rotation angle and also pushes the peak past the one obtained for a lower bias. In addition, the Kerr angle is negative in the same frequency range for which the permeability plots dip below the zero mark (see Fig. 5). The inset in (a) quantitatively assesses the ellipticity of the reflected beam and a profile in agreement with that of the Kerr rotation. The Faraday rotation in (b) which quantifies the plane of rotation of electric field for transmitted waves exhibits a similar behavior for a higher gate bias and records a minimum at the same frequency as noted for its Kerr counterpart. Note that the Kerr and Faraday rotation and the measure of ellipticity are evaluated using the transmission formalism whose governing equations are summarized in Eq. (14) in the main text. The material system used in these calculations is a 30.0 nm wide InSb well under an external magnetic field of 0.8 T and intrinsic magnetization of 0.3 T. The Gilbert damping constant, as usual, is set to 0.04.

where $\theta_{F/K}$ is the Faraday/Kerr rotation and $\eta_{F/K}$ stands for the ellipticity of the $p$-polarized wave. Note that the Fresnel coefficients can be in general complex quantities as seen from the form of Eq. (14). Moreover, $\theta_F = \text{Re}[\tan^{-1}(t_{ps}/t_{ss})]$, with a similar relation holding for $\theta_K$, the Kerr rotation.

This brief digression aside, which outlined the steps underpinning a numerical assessment of the Faraday and Kerr rotation, it is now possible to study their dependence on the $g$ factor that impacts the permeability tensor. We show such a calculation in Fig. 4 and elucidate further: First of all note that both $\theta_K$ and $\theta_F$ shift with an electric field, an observation easily reconcilable by recalling that the $g$ factor (via the RSOC) undergoes a change leading to a quantitatively different permeability tensor (cf. Fig. 5). It is therefore of interest that an electric (gate) field by acting upon the spin of the electrons for a given magnetic field arrangement (applied and intrinsic) serves as an effective control mechanism to regulate the $\theta_F$-governed figure of merit ($\zeta$) for magneto-optical devices. It is pertinent to mention here that the key to the adaptability of a nonreciprocal photonic device design is the $\zeta$ parameter, whose optimization until now has relied on the macroscopic alignment of the total angular momentum of magneto-optical ions (magneto-optical effects are principally an outcome of electronic states with different angular momentum) as a pathway to a high Faraday rotation. A typical arrangement generally brings into play a combined role for the intrinsic spin-orbit coupling of the magneto-optical material and an external magnetic field to achieve a $\zeta$ commensurate
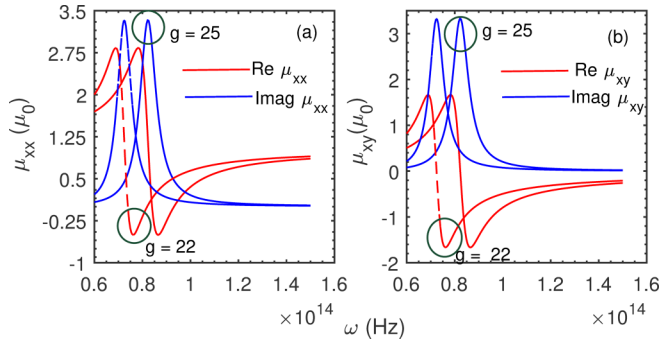
FIG. 5. The permeability dispersions for two different values of the *g* factor, where we made use of Eq. (4) and set the external *z*-axis directed magnetic field to 0.8 T, are shown in the above plots. The dispersion curves that use a *g*-factor value of 22 (25) are depicted by a dotted (solid) set of lines. Additionally, the intrinsic magnetization (parallel to the external magnetic field) and the dimensionless Gilbert damping constant were assumed to be 0.3 T and 0.04, respectively. The dispersion on the left (a) shows the real and imaginary components of the diagonal elements of the permeability tensor while the right panel (b) furnishes the corresponding curves for the off-diagonal entries. Note that the dispersions for both the diagonal and off-diagonal components besides displaying a functional dependence on the *g* factor also peak at a resonant frequency. A switch of signs is also observed for a frequency range in both cases.

with a level desirable for applications. While in principle a magnetic-field-controlled adjustment of material properties is feasible, electromagnetic compatibility and its lack thereof with the adjoining integrated circuitry (in a device environment) make it a less propitious design guideline. The suggested procedure in this work also involves control of the spin-orbit coupling (external) for a higher Faraday rotation, but with an electric bias that significantly mitigates the severity of electromagnetic incompatibility in the case of a magnetic field.

## IV. SPIN-POLARIZED PURCELL EFFECT AND THE *g* FACTOR

We showed how a recalibration of the permeability tensor via an altered *g* factor offers promise of tangible dynamic control in magneto-optical measurements. The genesis of such results, which lay in a rearrangement of the surrounding electromagnetic field, can also be observed in a different setting—the Purcell effect (PE). This effect is characterized by alterations to the spontaneous emission lifetime of a quantum source whose dynamical properties are induced by its interaction with the environment. From an application standpoint, the PE aids in the construction of nanoscale probes and development of newer light sources, for example, lasers and LEDs. The quantitative prediction of the PE is useful, therefore, especially where emission-controlled design parameters are of importance. A traditional approach to securing an optimal PE draws upon the geometry and optical attributes of the medium surrounding the emitter, notably, the electromagnetic local density of states (LDOS), determined in part by the constitutive parameters, $\epsilon$ and $\mu$. Here, to exemplify the role of the *g* factor in amendments to the PE, we consider a dipole placed close to the InSb slab and numerically compute the emitter (dipole) decay rate. Nominally, for a dipole moment **p** located at a distance $z_0$ above the first interface, the PE can be written as [25] (the frequency and speed of light in vacuum are $\omega$ and $c$, respectively)

$$P = 1 + 6\pi\epsilon_0 \frac{\mathrm{Im}\,\mathbf{p}^* \overline{\overline{\mathbf{G}}}_{\mathrm{scat}}(z_0)\mathbf{p}}{\omega^3 c^{-3}|\mathbf{p}|^2}, \quad (15a)$$

where $\overline{\overline{\mathbf{G}}}_{\mathrm{scat}}(z_0)$ is the scattered dyadic Green's function of the dipole near the InSb slab that starts at $z = 0$ and extends below. We write it as

$$\overline{\overline{\mathbf{G}}}_{\mathrm{scat}}(z_0) = \frac{i}{8\pi^2}\int \frac{d^2\mathbf{k}_\parallel}{k_z}\left[\overbrace{e^{i2k_z z_0}\underbrace{\left[(r_{ss}\hat{\mathbf{e}}_{s+} + r_{ps}\hat{\mathbf{e}}_{p+})\hat{\mathbf{e}}_{s-}^T\right]}_{\text{reflection of } \hat{\mathbf{e}}_{s-} \text{ wave}} + \underbrace{(r_{sp}\hat{\mathbf{e}}_{s+} + r_{pp}\hat{\mathbf{e}}_{p+})\hat{\mathbf{e}}_{p-}^T}_{\text{reflection of } \hat{\mathbf{e}}_{p-} \text{ wave}}}^{\text{scattered/reflected part } \overline{\overline{\mathbf{g}}}_{\mathrm{ref}}}\right], \quad (15b)$$

where $k_z = \sqrt{k_0^2 - k_\parallel^2}$. A plot of the Purcell factor ($F_p$) that features the decay rate of the dipole ($d_1 = 1/\sqrt{2}[x + iy]$) in the vicinity of the InSb slab (which serves as a model two-dimensional array of scattering centers) normalized to its value in free space is presented in Fig. 6. Clearly, as the *g* factor is increased, changing the localized electromagnetic setting through the $\mu$ tensor, a stronger field-dipole interaction is revealed as a concomitant rise in the Purcell factor. Further, we carried out the same calculation for a second orientation of the dipole ($d_2 = 1/\sqrt{2}[x - iy]$), which yielded no definitive gain for the $F_p$. A marginal rise in the decay rate (or equivalently the $F_p$) for both values of the *g* factor points to no significant modification of the localized electric field in presence of the $d_2$ dipole placed above the InSb slab.

We make a comment on the connection of the Purcell effect to the nonreciprocity of the optical medium. First, notice that the scattering matrix in the Purcell formulation identified through the dyadic Green's function [Eq. 15(b)], say for the dipole $d_1 = 1/\sqrt{2}[x + iy]$, is related to dipole $d_2 = d_1^*$ through the simple relation

$$\overline{\overline{\mathbf{G}}}_{\mathrm{scat}}(z_0, d_1) = \overline{\overline{\mathbf{G}}}_{\mathrm{scat}}(z_0, d_2) = \overline{\overline{\mathbf{G}}}_{\mathrm{scat}}^T(z_0, d_1). \quad (16)$$

The above relation, however, is untrue in a nonreciprocal medium such that the Purcell factors for dipoles $d_1$ and $d_2$ are unequal. Furthermore, since the two dipoles are distinguished through the spins of their emitted light [see Fig. 6(a) and accompanying caption] and display contrasting behavior, it is
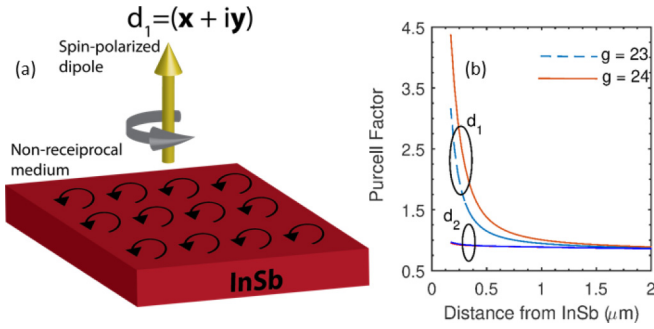
FIG. 6. The numerically determined Purcell factor ($F_p$) for two sets of circularly polarized dipoles of opposite handedness ($d_{1,2} = 1/\sqrt{2}[x \pm iy]$) placed at a certain distance from a 30.0 nm InSb slab with (assumed) intrinsic magnetization is shown here. We select two values of the $g$ factor for this calculation, where the lower (higher) number corresponds to an electric field of 8 (5) $\times 10^6$ V/m. For the case of the $d_1$ dipole, a large enhancement in the Purcell factor is observed, which correlates with an increase in the electromagnetic density of states arising from a constructive interference of electric field in the vicinity of the dipole, $d_1$. The placement of the second dipole ($d_2$), however, in contrast, leads to no significant uptick in the electric field and the $F_p$ remains close to unity. The $F_p$ also in the case of the $d_1$ dipole reaches a higher value for a $g$ factor pushed upward through a stronger gate bias. For smaller distances ($z_0$) from the slab, a more intense electric field operates that gives rise to a more robust $F_p$ uptick; this trend falls off for larger $z_0$ values in agreement with the usual inverse square law for electric fields. Note that the arrow curving around the dipole $d_1$ in panel (a) represents the emission of a right circularly polarized light; for $d_2$, the sense of polarization of emitted light is the exact opposite.

conceivable to view this as an instance of photonic spin tied to nonreciprocity.

## V. FINAL REMARKS

We explored the prospects of magneto-optical devices that epitomize the phenomenon of nonreciprocity [5] and showed that a newer class of design guidelines can be laid down wherein the electron's spin degree of freedom is the primary determinant through the inclusion of the external Rashba spin-orbit coupling (RSOC) assisted $g$ factor. A set of further advancements can be planned in which the usually weaker Dresselhaus spin-orbit coupling may actively influence the $g$ factor in tandem [39,40] with RSOC, and therefore requires an examination of a large variety of material systems using *ab initio* techniques. In addition, pursuant to the former objective of suitable candidate materials, a more systematic study of the current setup will aid us in quantitatively correlating (via first-principles simulations) various sample slabs of InSb with strain, magnetized dopants, defects, and vacancies to magneto-optical phenomena discussed here. Here, we may note that perovskites and their thin-film derivatives which are strongly magnetoelectric [41,42] and can carry a robust RSOC are an encouraging alternative as a starting point for further expanding the design space of magneto-optical structures [and upgrading the figure-of-merit ($\zeta$) parameter] through a conjoined action of the principles of multiferroics and electron spin-orbit coupling.

TABLE I. Eight-band $k \cdot p$ parameters for InSb. $E_v$, $E_g$, $E_p$, and $V_{so}$ are in units of eV. The remaining Luttinger parameters are dimensionless constants, and the effective mass is in units of the free electron mass.

| Material | $E_v$ | $\gamma_1$ | $\gamma_2$ | $\gamma_3$ | $m^*$ | $E_g$ | $E_p$ | $V_{so}$ |
|---|---|---|---|---|---|---|---|---|
| InSb | 0.28 | 34.8 | 15.5 | 16.5 | 0.0135 | 0.235 | 18 | 0.81 |

The theme of nonreciprocity allied to photon spin was carried over to Purcell factor calculations, where we established using the theory of the dyadic Green's function the decay rate of a dipole held close to an InSb slab. This framework also allows us to assess situations with a randomized configuration of electromagnetic scatters or plasmonic nanoantennas replacing the InSb slab, essentially building a general theory of decay rates in a Purcell factor calculation of emitters (dipoles) near a 2D array of scattering centers. A more comprehensive set of results that suggests structures and emitter orientations maximizing the Purcell effect is planned for a future publication.

## APPENDIX: BAND STRUCTURE CALCULATIONS

We include material that was left out of the main text and brief explanatory notes that clarify and expand on the discussion presented in the paper. The 8-band $k \cdot p$ band structure calculations are performed by discretizing the InSb slab (modeled as a quantum well) on a cubic grid. The
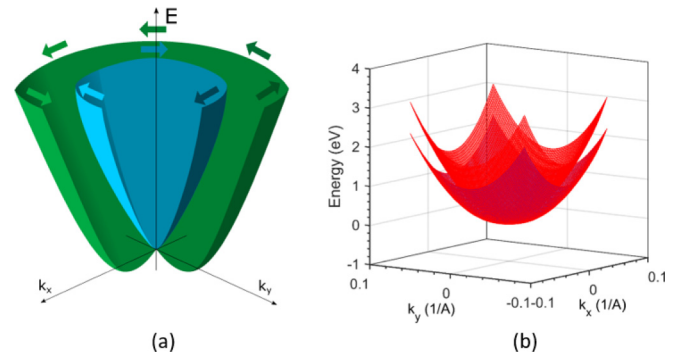


FIG. 7. The Rashba spin-orbit coupling (RSOC) leads to two nondegenerate Fermi concentric energy contours for the spin-up and spin-down ensemble (a). The right panel (b) shows the band structure of conduction electrons of a 6.0 nm InSb quantum well obtained from a $k \cdot p$ calculation. The two "winged profiles" in the right panel (b) denote the energy contours for the spin-up (higher energy) and spin-down electrons. Notice that InSb is an ideal candidate material to observe RSOC as it satisfies the twin criteria of a large intrinsic spin-orbit coupling (0.78 eV) and a small band gap (0.43 eV at Brillouin zone center). In the present case, the Rashba coupling parameter was artificially enhanced to 4.0 eV Å for a more vivid portrayal of the spin splitting.

quantum well is assumed to be grown along the [001] axis. The quantized direction is aligned to [001] which is also the $z$ axis. The InSb slab Hamiltonian, $H(k_x, k_y, -i\frac{\partial}{\partial z})$, is of size $8N_z \times 8N_z$, where $N_z$ represents the number of discretized points along the $z$ axis. The finite-difference discretization scheme for the 8-band $k \cdot p$ Hamiltonian has been explained fully in Ref. [10]. The $k \cdot p$ parameters for this work were obtained from Vurgaftman *et al.* [43]. The parameters are also collected in Table I for easy reference. The conduction band profile of a 6.0 nm InSb quantum well which is spin-split by the Rashba coupling is shown in Fig. 7. In preparing Fig. 7, the effective mass [cf. Eq. (5)] of the conduction electrons was obtained from the 8-band $k \cdot p$ calculation.

A direct approach to ascertain the $g$ factor [$g_f$ in Eq. (A1)] using $k \cdot p$ theory is from the following result:

$$g_f = g_0 \left[ 1 - \frac{E_p}{3} \left( \frac{1}{E_{6c} - E_{8v}} - \frac{1}{E_{6c} - E_{7v}} \right) \right]. \quad \text{(A1)}$$

In Eq. (A1), $g_0 \approx 2$ is the free electron $g$ factor while the subscripts $6c$, $7v$, and $8v$ designate the symmetries of the bottom (top) of the conduction (valence) bands in a crystal with $T_d$ symmetry. All remote contributions from higher-order bands have been ignored. Note that $E_{6c} - E_{8v}$ is the fundamental band gap ($E_g$) and $E_{6c} - E_{7v} = E_g + \Delta_{so}$. Here, $\Delta_{so}$ is the splitting from the intrinsic spin-orbit coupling. While in principle it is possible to derive a similar expression with the Rashba coupling term that explicitly accounts for $E_g$, $\Delta_{so}$, and the effective mass, the approximate estimation procedure outlined in Sec. II A indirectly includes the foregoing quantities through the Rashba parameter [cf. Eq. (8)].

Finally, in the context of the 8-band $k \cdot p$ Hamiltonian based $g$-factor calculations, it is relevant to mention here that the use of only the lowest conduction band is a reasonable approximation for InSb; the next $p$-like conduction band ($\Gamma_7$) is much above the fundamental direct band gap. A more accurate model, however, must include the $\Gamma_7$ and $\Gamma_8$ conduction bands, for instance, in GaAs, suggesting a 14-band $k \cdot p$ calculation as our starting point. The $g$-factor formula [Eq. (A1)] must reflect this modification through terms of the form of [33].

[1] A. Eroglu, *Wave Propagation and Radiation in Gyrotropic and Anisotropic Media* (Springer Science & Business Media, New York, 2010).

[2] A. Kamal, J. Clarke, and M. Devoret, Nat. Phys. **7**, 311 (2011).

[3] L. Bi, J. Hu, P. Jiang, D. H. Kim, G. F. Dionne, L. C. Kimerling, and C. Ross, Nat. Photonics **5**, 758 (2011).

[4] J. Kong, *Electromagnetic Wave Theory* (Wiley Interscience, New York, 1986).

[5] M. G. Silveirinha, Phys. Rev. B **95**, 115103 (2017).

[6] S. Pendharker, F. Kalhor, T. Van Mechelen, S. Jahani, N. Nazemifard, T. Thundat, and Z. Jacob, Opt. Express **26**, 23898 (2018).

[7] S. M. Barnett, New J. Phys. **16**, 093008 (2014).

[8] S. A. R. Horsley, Phys. Rev. A **98**, 043837 (2018).

[9] T. Van Mechelen and Z. Jacob, Opt. Mater. Express **9**, 95 (2019).

[10] T. Van Mechelen and Z. Jacob, Phys. Rev. A **98**, 023842 (2018).

[11] T. Van Mechelen and Z. Jacob, Phys. Rev. B **99**, 205146 (2019).

[12] T. Van Mechelen and Z. Jacob, Nanophotonics **8**, 1399 (2019).

[13] L. Zhu, Y. Guo, and S. Fan, Phys. Rev. B **97**, 094302 (2018).

[14] C. Khandekar and Z. Jacob, New. J. Phys. **21**, 103030 (2019).

[15] T. Van Mechelen and Z. Jacob, Optica **3**, 118 (2016).

[16] P. Sengupta, H. Ryu, S. Lee, Y. Tan, and G. Klimeck, J. Comput. Electron. **15**, 115 (2016).

[17] R. F. Van Welzenis and B. Ridley, Solid-State Electron. **27**, 113 (1984).

[18] K. Chen, P. Santhanam, S. Sandhu, L. Zhu, and S. Fan, Phys. Rev. B **91**, 134301 (2015).

[19] E. Kamenetskii, IEEE Trans. Antennas Propag. **49**, 361 (2001).

[20] F. Lima, T. Dumelow, E. Albuquerque, and J. Da Costa, J. Opt. Soc. Am. B **28**, 306 (2011).

[21] Y. Tang and A. E. Cohen, Phys. Rev. Lett. **104**, 163901 (2010).

[22] I. Žutić, J. Fabian, and S. D. Sarma, Rev. Mod. Phys. **76**, 323 (2004).

[23] A. Manchon, H. C. Koo, J. Nitta, S. Frolov, and R. Duine, Nat. Mater. **14**, 871 (2015).

[24] P. N. Argyres, Phys. Rev. **97**, 334 (1955).

[25] L. Novotny and B. Hecht, *Principles of Nano-optics* (Cambridge University Press, Cambridge, 2012).

[26] F. Khosravi, C. L. Cortes, and Z. Jacob, Opt. Express **27**, 15846 (2019).

[27] M. Lakshmanan, Philos. Trans. R. Soc. London A **369**, 1280 (2011).

[28] Y. Tserkovnyak, A. Brataas, and G. E. W. Bauer, Phys. Rev. Lett. **88**, 117601 (2002).

[29] L. D. Landau, J. Bell, M. Kearsley, L. Pitaevskii, E. Lifshitz, and J. Sykes, *Electrodynamics of Continuous Media* (Elsevier, New Delhi, 2013).

[30] J. Hübner, S. Döhrmann, D. Hägele, and M. Oestreich, Phys. Rev. B **79**, 193307 (2009).

[31] B. Nedniyom, R. J. Nicholas, M. T. Emeny, L. Buckle, A. M. Gilbertson, P. D. Buckle, and T. Ashley, Phys. Rev. B **80**, 125328 (2009).

[32] R. Winkler, *Spin-Orbit Coupling in Two-Dimensional Electron and Hole Systems* (Springer, Berlin, 2003).

[33] C. Hermann and C. Weisbuch, Phys. Rev. B **15**, 823 (1977).

[34] C. E. Pryor and M.-E. Pistol, J. Appl. Phys. **118**, 225702 (2015).

[35] S. Jacobs, K. Teegarden, and R. Ahrenkiel, Appl. Opt. **13**, 2313 (1974).

[36] G. Széchenyi, M. Vigh, A. Kormányos, and J. Cserti, J. Phys.: Condens. Matter **28**, 375802 (2016).

[37] A. Ishimaru, S.-W. Lee, Y. Kuga, and V. Jandhyala, IEEE Trans. Antennas Propag. **51**, 2550 (2003).

[38] H. Da, Q. Bao, R. Sanaei, J. Teng, K. P. Loh, F. J. Garcia-Vidal, and C.-W. Qiu, Phys. Rev. B **88**, 205405 (2013).

[39] D. V. Bulaev and D. Loss, Phys. Rev. B **71**, 205324 (2005).

[40] L. Meier, G. Salis, I. Shorubalko, E. Gini, S. Schön, and K. Ensslin, Nat. Phys. **3**, 650 (2007).

[41] L. Yan, Y. Yang, Z. Wang, Z. Xing, J. Li, and D. Viehland, J. Mater. Sci. **44**, 5080 (2009).

[42] E. Bousquet and N. Spaldin, Phys. Rev. Lett. **107**, 197603 (2011).

[43] I. Vurgaftman, J. R. Meyer, and L. R. Ram-Mohan, J. Appl. Phys. **89**, 5815 (2001).